

Trabalho de Conclusão de Curso

Pt Doping Effects on $TiSe_2$ Catalytic Activity Towards Hydrogen Evolution Reactions

Caique Campos de Oliveira^{1,*} and Pedro A. S. Autreto¹

¹*Centro de Ciências Naturais e Humanas,
Universidade Federal do ABC, Santo André-SP, Brasil*

Hydrogen (H_2) generation *via* the Hydrogen Evolution Reaction (HER) mechanism has increasingly attracted researchers interest in the last few years. Since the works of Hinnemann *et al.* [1] and Jaramillo *et al.* [2] that demonstrated the prominent catalytic activity of MoS_2 (close to that of Pt), Transition Metal Dichalcogenides (TMDs) has emerged as one of the main materials studied in catalysis. Despite the great fame of MoS_2 , $TiSe_2$ has also emerged as a TMD with unique electronic and structural properties for various applications. Previous works demonstrated that doping (among other techniques) could significantly enhance TMD catalytic activity towards HER. In this work, we analyze the effects of the introduction of Pt doping on $TiSe_2$ catalytic activity using Density Functional Theory (DFT). We employed the Computational Hydrogen Electrode model to use the free energy of Hydrogen adsorption (ΔG_{H^*}) as a physical descriptor of the catalytic performance.

1. INTRODUCTION

Fossil fuels mainly supply the energetic global mix, with oil, coal, and natural gas taking up to 84% of the total blend while renewable sources such as solar and wind sum up to only 4%. Hydro, nuclear, and biomass complete this composition [3]. However, fossil fuels are a limited resource, and their reserves are restricted to some areas of the globe (see Ref. [3]). In addition, the energy content of these fuels is released through combustion, and as these compounds are mainly Hydrocarbons, producing greenhouse gases (GHG) such as CO_2 , which is one of the main contributors to the global warming [4].

The large-scale exploitation of non-renewable sources and environmental consequences of fossil-fuel consumption (air pollution and global warming) urges the need for clean and renewable energy sources. Hydrogen is one of the most promising energy carriers, offering incredible energy per unit

*Electronic address: caique.campos@aluno.ufabc.edu.br

mass content (120 kJ.g^{-1})[5]. It is considered a clean energy carrier with transport and security advantages over fossil-fuels [6, 7]. In spite of the large abundance of this element, molecular Hydrogen (H_2) is not available in nature and must be produced.

Current methods for H_2 production are based on fossil fuel reformings, such as steam reforming employed to convert H from light hydrocarbons (natural gas) or partial oxidation, which employs heavier hydrocarbons from oil or coal as feedstock. However, both reforming methods produce carbon oxides far from the clean approach to produce H_2 . Another method that uses fossil fuels is pyrolysis which decomposes hydrocarbons in H_2 , and C [8]. Green H_2 production powered by clean energy sources enables renewability. It makes Hydrogen one of the most promising energy carriers/sources for the future, with the potential to decarbonize almost 20% of the energetic consumption by the introduction in chemistry, transport, and residential sectors [9].

Clean H_2 production can be achieved by the water-splitting process, whereby water molecules are decomposed into hydrogen (H_2) and oxygen (O_2) through redox reactions [6, 10]. This process can be powered by electric, mechanical, photonic, or thermal energy [11]. In particular, H_2 production by water electrolysis in the electrochemical *Hydrogen Evolution Reaction* (HER) is one of the most often studied mechanisms [12] due to the possibility of being powered by clean and renewable electricity and the high purity H_2 yield [13]. This mechanism is briefly discussed next.

1.1. Hydrogen Evolution Reaction

Water splitting by electrolysis is the electrochemical process in which electric power is converted to chemical energy. The water molecule is dissociated, and its atoms recombined to form hydrogen (H_2) and oxygen (O_2). The overall reaction ($H_2O \rightarrow H_2 + \frac{1}{2}O_2$) is powered by electricity in electrochemical cells (also known as electrolyzers) and is divided in two semi-reactions: the *Hydrogen Evolution Reaction* (HER) occurring in the cathode and the *Oxygen Evolution Reaction* (OER) on the anode [14]. The actual reaction in these steps depends on environmental conditions such as pH [12, 15]. Nonetheless, it always involves electrons transfers. In acidic media, OER and HER semi-reactions are written as [14]:



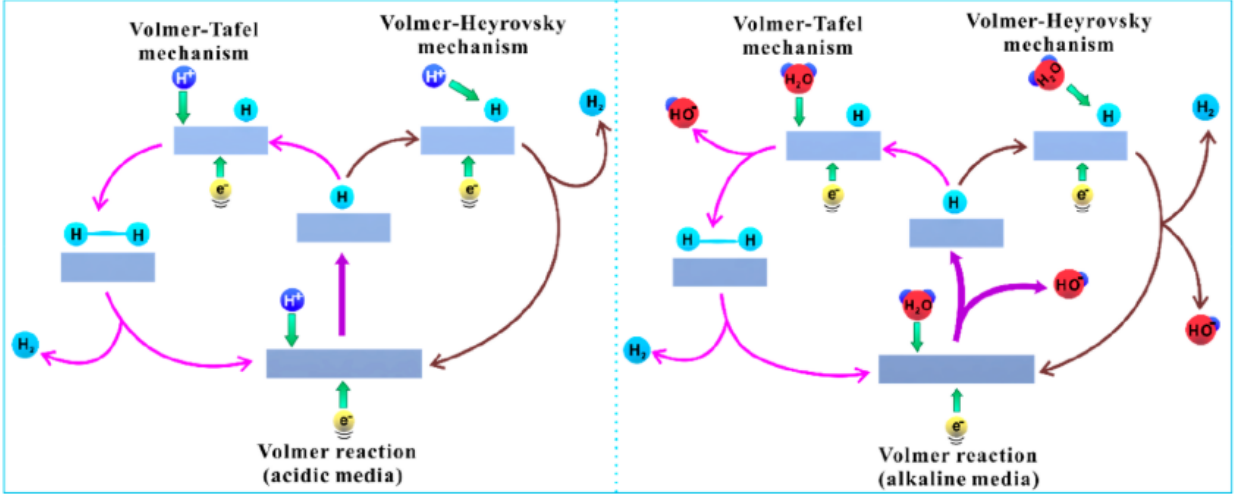


FIG. 1: Mechanism of HER in acidic media (left) and alkaline media (right). Reproduced from [17].

respectively, whereas the alkaline semi-reactions are [12, 16]:



The cathodic HER is one of the most studied mechanisms for clean and renewable H_2 production [10, 12, 14, 17, 18]. It begins with a reaction between a proton and an electron, forming an adsorbed Hydrogen atom at the electrode surface (H^*). This step is known as the *Volmer* step. In acidic media, the protons are provided by Hydronium (H_3O^+), whereas in alkaline electrolytes, they are provided by H_2O molecules [17]. The second step of the reaction is the desorption that can occur by an electrochemical reaction (*Heyrovsky* step) in which an H^* interacts with a proton and an electron, yielding a H_2 molecule. The desorption can also proceed *via* chemical reaction (the *Tafel* step), where two neighboring H^* combine to form the H_2 [14, 19]. A illustration of this mechanism is shown in Fig. 1.

In acidic media, the reaction can involve the three steps mentioned above, which leads to the following set of equations representing the Volmer, Heyrovsky, and Tafel steps, respectively:



In alkaline media, the desorption occurs only by the Heyrovsky step [10], leading to the following set of equations:



To trigger the reaction, an energy barrier (the *overpotential* - η) has to be overcome. Large overpotentials of the semi-reactions are one of the limiting factors of this mechanism [19, 20], along with mass-transport losses in H_2 produced [21]. Efficient H_2 generation by HER requires minimizing this overpotential and enhancing the reaction kinetics, which is accomplished by using catalysts. As the reaction forms and breaks bonds between catalyst active sites and H, the catalytic activity is strongly correlated to the adsorption and desorption energies of the reactants and the products, respectively [22]. By correlating kinetic parameters of the reaction with physical properties of the catalyst Nørskov *et al.* compared the measured electric current density (j_0) versus the calculated Gibbs free energy of the adsorbed Hydrogen (ΔG_{H^*}) for a series of metals, resulting in a volcano plot pointing to the maximum j_0 when $\Delta G_{H^*} = 0$ [23].

The Hydrogen Binding Energy (HBE) plays a crucial role and ΔG_{H^*} provides insights into the efficiency of the catalyst. When ΔG_{H^*} is a large positive value ($\Delta G_{H^*} > 0$), H binds weakly into the catalyst surface. Therefore the Volmer step is limited, compromising the evolution to H_2 . In practical terms, this means that the catalyst dissociates and adsorb protons (H^+) from H_3O^+ or H_2O poorly. When ΔG_{H^*} is a large negative value ($\Delta G_{H^*} < 0$), the H binds strongly to the active site of the catalyst, thus limiting the desorption steps. This solid binding causes the permanent occupation of the active sites and, therefore, poisoning of the catalyst [19].

When designing new catalysts for HER, it is necessary to consider the conditions in which the electrolysis takes place. In acid media, the mechanism employs a *Proton Exchange Membrane* (PEM) that offers high energy efficiency and fast H_2 production rate. The downside is that it demands noble-metals and noble-metal oxide-based catalysts [8, 10]. Alkaline electrolysis offers a broad range of catalysts (non-noble metals and their oxides) at the cost of performance. HER activity in alkaline media is 2-3 orders of magnitude less than in acid media [15] even for benchmark catalysts such as *Pt*. This difference is usually attributed to the sluggish water dissociation step [10]. Acid HER offers better performance than the previous, and is relatively simpler, consisting only of protons reduction (Eq 2) being the main focus of this work.

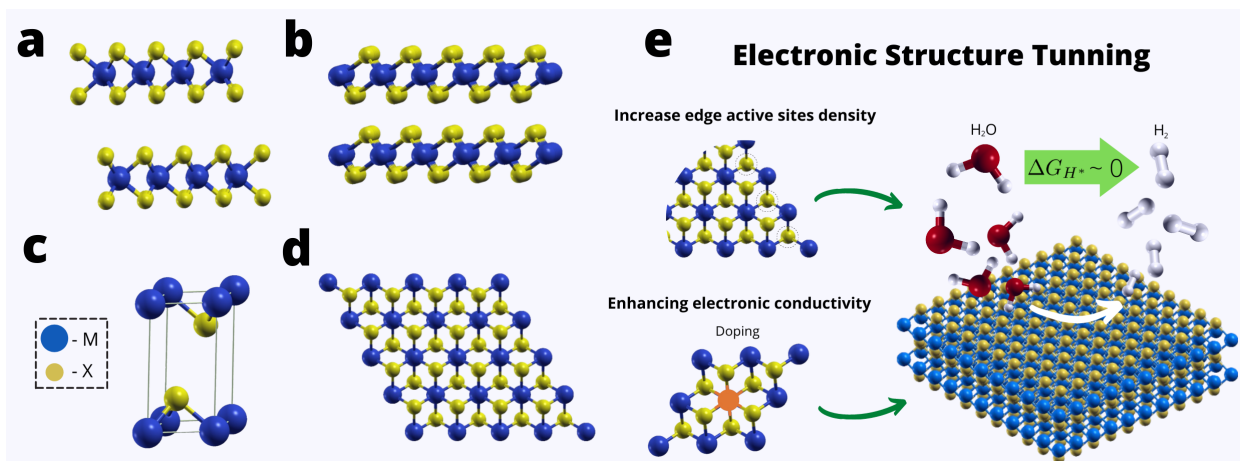


FIG. 2: General structure of (a) $2H$ and (b) $1T$ phases for TMDs. In (c) the hexagonal of $1T$ - $TiSe_2$ and its basal plane (001) for a 4×4 supercell. In (e) a scheme of the most common strategies used to enhance TMDs catalytic activity (own authorship).

1.2. Catalysts for HER

Up to date, noble-metal based materials such as *Pt*, *Ir* and *Pd* exhibit the best catalytic activity in HER [24]. *Pt* is regarded as the reference catalyst achieving $\Delta G_{H^*} = 0.08$ eV [23]. However, noble-metal scarcity limits its large-scale application. In the last few years the research for cheap earth-abundant noble-metal free catalysts has drawn considerable attention and interesting alternatives has been proposed. Among them, the Transition Metal Dichalcogenides (TMDs) has emerged as an effective alternative, due to interesting structural and electronic properties [14, 19, 25]. These compounds exhibits a general MX_2 formula with a transition metal (M) covalently bonded to two chalcogen (X) atoms, forming layered sequences $X-M-X$ which stack upon each other by weak van der Waals interactions (Fig. 2.a,b) [19].

The wide variety of compositions renders various electronic properties to these materials, which exhibit metallic, semi-metallic, and semiconductor behavior [26]. They crystallize in the most common $1T$ and $2H$ phases (Fig. 2.a,b respectively) and can undergo a phase transition by intercalation with other elements [27], induced by pressure [28] and by mechanical strain [29] affecting electronic and structural properties [30]. The $2H$ MoS_2 for example display a 1.2 eV band-gap being a semiconductor while the $1T$ MoS_2 exhibit metallic behavior [31].

The basal plane of TMDs displays a significant amount of potential sites for catalysis. However, for semiconducting TMDs, as MoS_2 for example, many of these sites are inert and the active sites are located in the edges [2]. The $2H$ MoS_2 displays a remarkable activity ($\Delta G_{H^*} = +0.08$ eV)

[1, 2], but the low amount of edge sites limit its performance. On the other hand, the transition to the $1T$ phase significantly improves the reaction kinetic, boosting its catalytic activity, even though being a metastable phase [31, 32]. The main strategies to optimize TMDs catalytic performance in HERs are related to increasing the number of active sites and enhancing electronic and transport properties [19]. Most common techniques used are phase engineering and doping [33, 34].

Among TMDs Titanium Disselenide ($TiSe_2$) has attracted great interest of research due to its unique electronic properties including ordered electronic states (CDW) [35] and superconductivity [36] with great potential to a range of applications. The $1T$ phase is more thermodynamic stable exhibiting metallic behavior [37, 38]. Interlayer spacing (0.611 nm) [39] results in good electronic conductivity, thermodynamic stability and facilitates exfoliation into few/mono layers [37, 40]. $1T$ $TiSe_2$ undergo a CDW transition at $T_c = 202K$ [41], from ambient pressure until 2 GPa [28] with a $2 \times 2 \times 2$ ($a = 2a_0$ e $c = 2c_0$) super-lattice formation [35]. Its electronic properties are sensible to both Se deficiency and doping, resulting in a higher resistivity at elevated temperatures. In the absence of Se deficiency, doping results in a lower resistivity, boosting the metallic character [39].

In this work, we investigate the effects of heteroatom introduction (doping) in the catalytic activity of $1T$ $TiSe_2$ in HER using first-principles calculations based on DFT. The HER is modeled using the Computational Hydrogen Electrode (CHE). This model enables the thermodynamic study of HER in terms of free energy variation for intermediate states. We perform geometry optimization and surface energy convergence calculations and investigate the activity of basal plane (001) sites in both pristine and doped structures. We also elaborate charge density difference plots to visualize the charge distribution on the adsorbed Hydrogen. Our final results are compiled in free energy diagrams.

2. METHODOLOGY

2.1. Density Functional Theory

The non-relativistic quantum description of a physical system is given by Schödinger's equation (Eq. 10) whose solutions gives the wavefunctions ($\Psi(\vec{r}, t)$) containing all information for each

particle.

$$i\hbar \frac{\partial}{\partial t} \Psi(\vec{r}, t) = \hat{H} \Psi(\vec{r}, t) \quad (10)$$

Physicists often separate time and spatial variables splitting the original partial differential equation into two ordinary equations. The stationary (Eq. 11) and temporal (Eq. 12) equations are much more simpler to handle because they involve only on variable. When we calculate the expected value of an observable A , the integral of the temporal contribution ($\phi^*(t)A\phi(t)$) over the phase-space vanishes, leaving only the spatial part.

$$\hat{H}\psi(\vec{r}) = E\psi(\vec{r}) \quad (11)$$

$$i\hbar \frac{\partial}{\partial t} \phi(t) = E\phi(t) \quad (12)$$

In complex systems such as molecules or solids, electrons and nuclei interact with each other. However, electrons are much more sensitive to changes in their neighboring because they are much lighter than nuclei. Therefore, it is reasonable to consider atomic nuclei as fixed (the atomic nucleus is not static due to the uncertainty principle). This assumption —known as the *Born-Oppenheimer* approximation [42] —simplifies the Hamiltonian (H), because the kinetic energy of nuclei vanishes and their electrostatic repulsion is constant. Consequently, Schrödinger's equation can be solved for the electrons motion in a potential generated by a collection of nuclei (V_n), providing the ground state energy [43].

For time-independent potentials ($V_n = V_n(\vec{r}_i)$) the Hamiltonian of such a system is given by:

$$\hat{H} = \frac{\hbar^2}{2m_e} \sum_i r_i^2 + \sum_i V_n(\vec{r}_i) + \sum_{i<j} U(\vec{r}_i, \vec{r}_j) \quad (13)$$

the first term describes the kinetic energy of the electrons. The second one the electrostatic interaction between an electron and a collection of nuclei. The third term represents the electrostatic repulsion between electrons. \hbar is the reduced Planck's constant, and m_e the electron's rest mass.

The solutions for the stationary Schrödinger's equation (Eq. 14) for this Hamiltonian gives the all-electron (electronic) wavefunction ($\psi(\vec{r}_1, \vec{r}_2, \dots, \vec{r}_N)$), a function of the positions of all the electrons. The energy caculated by Eq. 14 is a function of fixed nuclei positions ($E(\vec{R}_1, \vec{R}_2, \dots, \vec{R}_N)$), which is known as the *adiabatic potential energy surface* [42]. If the form of this energy is known, is possible to analyze its behavior as nuclei are moved around and find the lowest energy (or the ground state energy - E_0) for the system.

$$\left[\frac{\hbar^2}{2m_e} \sum_i r_i^2 + \sum_i V_n(\vec{r}_i) + \sum_{i<j} U(\vec{r}_i, \vec{r}_j) \right] \psi = E\psi \quad (14)$$

To find a single electron wavefunction in Eq. 14, it is necessary to know the position of all the other electrons. Thus, $3N$ spatial coordinates are required to solve the problem. This formulation is known as the *many-body Schrödinger equation*. The solution for systems with a few dozens of atoms becomes very difficult, not to mention the tremendous computational resources needed to accomplish this task.

On the other hand, quantum mechanics states that only the square of the wavefunction ($|\Psi(\vec{r}_1, \dots, \vec{r}_N)|^2$) have a physical meaning —probability of finding electrons in a certain set of coordinates $(\vec{r}_1, \vec{r}_2, \dots, \vec{r}_N)$. As electrons are not distinguishable from each other, at the end of the day, the quantity of interest is the probability of finding a collection of electrons (in any order) at a certain set of positions, which can be computed with the *electronic density*:

$$\rho(\vec{r}) = N \int d^3\vec{r}_1 \dots \int d^3\vec{r}_N \Psi^*(\vec{r}_1, \dots, \vec{r}_N) \Psi(\vec{r}_1, \dots, \vec{r}_N) \quad (15)$$

1. Hohenberg-Kohn Theorem

Density Functional Theory (DFT) is built upon two theorems demonstrated by W. Kohn and P. Hohenberg in 1964. The first theorem states that the ground-state energy (E_0) of a electronic system is uniquely determined by a functional of the electronic density [44]:

$$E_0 = F[\rho] \quad (16)$$

The density is a functional of the electronic wavefunction (Eq. 15). The Hohenberg Kohn (HK) theorem states that for ground-state this relation can be inverted. Therefore, there is a functional relation between the ground-state electronic wavefunction (Ψ) and the density (ρ_0). As a consequence, all the ground-state observables are a functional of the electronic density [45]. Instead of find the electronic wavefunction ($\Psi(\vec{r})$), the ground-state energy of the system can be calculated with the electronic density ($\rho(\vec{r})$). This substitution reduces the problem from $3N$ to only 3 spatial variables.

According to the HK theorem, if the ground-state density (ρ_0) of the system is known, its energy (E_0) is determined. However, it does not tell us how to calculate this density. Hohenberg and Kohn demonstrated that the correct ρ_0 is the one that minimizes the functional F [44]. Moreover, the value of this functional at ρ_0 corresponds to the ground-state energy E_0 . This minimization is called the *Hohenberg Kohn variational principle* and is the second fundamental theorem for DFT,

expressed as:

$$\left. \frac{\delta F[\rho]}{\delta \rho} \right|_0 = 0 \quad (17)$$

It is important to note that the theorems only holds for the ground state. For excited states, we calculate the energy with the expected value of the Hamiltonian (\hat{H}):

$$E_n = \langle \Psi_n | \hat{H} | \Psi_n \rangle = F[\Psi_n] \quad (18)$$

Here, we used Dirac's bracket notation for the sake of simplicity. According to the Hohenberg-Kohn theorem, in the ground state, the electronic density (ρ) uniquely determines the external potential ($V_{ext}(\vec{r})$). For any state, this potential determines the electronic wavefunctions (Ψ), which ultimately determines the energy by Eq. 18 [43]:

$$E_0 = \langle \Psi_0 | \hat{H} | \Psi_0 \rangle = \langle \Psi[\rho_0] | (\hat{T} + \hat{W}) | \Psi[\rho_0] \rangle + \int d\vec{r} \rho_0(\vec{r}) V_n(\vec{r}) \quad (19)$$

The first term is an implicit function of ρ . It describes the kinetic and potential energy of interacting electrons whose form is unknown. The second term is an explicit functional of the density. In 1965, Kohn and Sham proposed splitting the energy for an interacting system into a known part plus the term accounting for the difference with the true value (labeled as E_{xc}). The known part is composed of the kinetic energy of a non-interacting system with the same density (labeled T_S) and the Hartree potential that describes electrons' repulsion of each other. The E_{xc} energy accounts for quantum effects such as exchange and correlation [46]:

$$\langle \Psi[\rho] | (\hat{T} + \hat{W}) | \Psi[\rho] \rangle = \langle \Psi[\rho] | T_S | \Psi[\rho] \rangle + \langle \Psi[\rho] | V_H | \Psi[\rho] \rangle + E_{xc} \quad (20)$$

The functional becomes:

$$F[\rho] = \frac{\hbar^2}{2m_e} \sum_i \int d\vec{r} \phi_i^*(\vec{r}) \nabla^2 \phi_i(\vec{r}) + \frac{1}{2} \iint d\vec{r} d\vec{r}' \frac{\rho(\vec{r})\rho(\vec{r}')}{|\vec{r} - \vec{r}'|} + \int d\vec{r} \rho(\vec{r}) V_n(\vec{r}) + E_{xc} \quad (21)$$

the first and second terms correspond to the explicit form of the expected values for T_S and V_H , respectively. It can be seen that T_S is not a explicit functional of the density but rather a functional of the Kohn-Sham eigenstates ϕ_i (presented next). These orbitals are functionals of ρ and this implicit relationship is denoted by $T_S[\rho] = T_S[\mathcal{F}\phi[\rho]\mathcal{G}]$ [45].

2. Kohn-Sham Equations

According to the second HK theorem, the ground-state energy (E_0) can be calculated by:

$$E_0 = \left. \frac{\delta F[\rho]}{\delta \rho} \right|_0 = 0 \quad (22)$$

where δ denotes the functional derivative. Introducing the orthonormal *Kohn-Sham (KS) wavefunctions*:

$$\rho(\vec{r}) = \sum_j |\phi_j(\vec{r})|^2 \quad (23)$$

$$\delta_{ij} = \int \phi_i^* \phi_j \quad (24)$$

we use the chain rule to rewrite the variational derivative in terms of the KS wavefunctions as:

$$\frac{\delta F}{\delta \rho} = \frac{\delta F}{\delta \rho} \frac{\delta \rho}{\delta \phi^*} = \frac{\delta F}{\delta \phi^*} \quad (25)$$

using Lagrange Multipliers [47] we minimize F with respect to the ϕ_i 's leading to the *Kohn-Sham equations* [46]:

$$\left[\frac{\hbar^2}{2m_e} \nabla^2 + V_n(\vec{r}) + \int d\vec{r}' \frac{\rho(\vec{r}')}{|\vec{r} - \vec{r}'|} + \frac{\delta E_{xc}}{\delta \rho} \right] \phi_i(\vec{r}) = \epsilon_i \phi_i(\vec{r}) \quad (26)$$

here, ϵ_i are the Kohn-Sham eigenvalues. It must be clear that the $\phi_i(\vec{r})$ are not the electrons wavefunctions although they give the correct electronic density (Eq. 23). In the same way, ϵ_i must be understood as the eigenvalues and not the energy, although they give a good estimate of the latter. The Kohn-Sham formalism treats DFT as a single particle theory but many-body effects still included *via* E_{xc} term [45].

3. Self-Consistent Calculations

In addition to the equations, Kohn and Sham proposed a *self-consistent* procedure to solve them [46]. By guessing an initial density ρ_0 , we construct $V_n(\vec{r})$, V_H and V_{ex} by Eqs. 28, 29 and 30 to build V_{eff} (Eq. 27). Then, we solve Kohn-Sham equations (Eq. 26) and use its eigenstates to calculate a new density ρ_{new} by Eq. 31. If the difference between ρ_0 and ρ_{new} is smaller than some convergence criteria, the calculation has achieved self-consistency and the ground state density has been found. Otherwise, ρ_{new} is used as an input in the following step, until self-consistency is

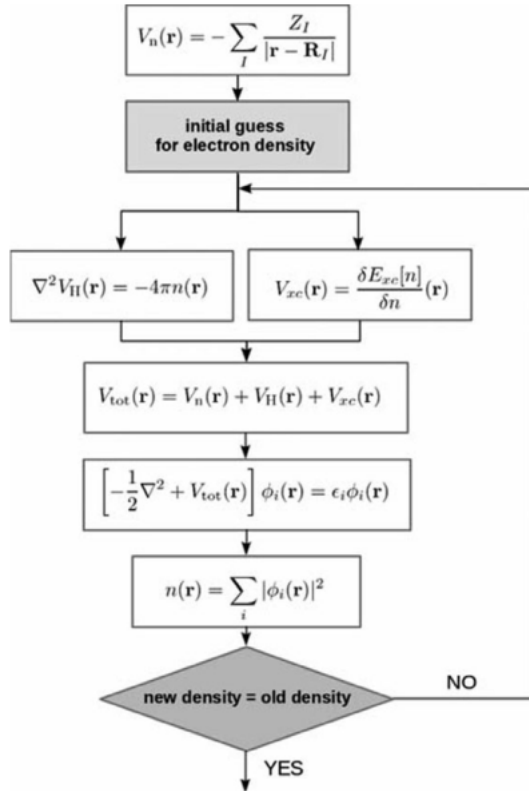


FIG. 3: Flowchart picturing the algorithm to find the self-consistent solutions for the Kohn-Sham Equations (Eq. 26). Reproduced from [43].

achieved. A schematic diagram of this *self-consistent* algorithm is shown in Fig. 3.

$$V_{eff} = V_n + V_H + V_{xc} \quad (27)$$

$$V_n = \sum_j \frac{Z_n}{|\vec{r} - \vec{r}_j|} \quad (28)$$

$$r^{-2} V_H = 4\pi\rho(\vec{r}) \quad (29)$$

$$V_{xc} = \frac{\delta E_{xc}[\rho]}{\delta\rho}(\vec{r}) \quad (30)$$

$$\rho(\vec{r}) = \sum_i |\phi_i(\vec{r})|^2 \quad (31)$$

4. Approximations for the Exchange and Correlation Energy

The real form of E_{xc} still a topic of research. However, there are good approximations with practical applications. The simplest approximation is built upon the local exchange energy for a Homogeneous Electron Gas (HEG ou *Jellium*) with the same density. The exchange energy ($E_x[\rho]$)

is given by Dirac's exchange formula (Eq. 32) [43, 48]. This formulation is known as the *Local Density Approximation* (LDA).

$$E_x^{LDA}[\rho] = \frac{3}{4} \left(\frac{3}{\pi} \right)^{\frac{1}{3}} \int_V \rho(\vec{r})^{\frac{4}{3}} d\vec{r} \quad (32)$$

For the correlation term (E_c), the energy for an electron ϵ_c can be determined analytically for theoretical limit cases ($\rho \rightarrow 0$ and $\rho \rightarrow \infty$). In the 1980, Ceperley and Alder used Monte Carlo numerical methods to simulate intermediate densities [49]. Various forms for E_c has been proposed based on extrapolation from Ceperley and Alder's data [48] since.

LDA does not account for local changes in ρ neither for the electron spin. In particular, spin contributions are included *via Local Spin Density Approximation* (LSDA), taking into account different spin states densities, in a way that the total density is written as:

$$\rho = \rho_{\downarrow} + \rho_{\uparrow} \quad (33)$$

The Exchange and correlation energy is now a functional of ρ and ζ , which describes the spin polarization ($\zeta = (\rho_{\downarrow} - \rho_{\uparrow})/\rho$). The LSDA form for E_{xc} is given in Eq. 34, where $\epsilon_{xc}[\rho, \zeta]$ is the exchange and correlation energy per particle in a uniform electron gas [50].

$$E_{xc}^{LSDA}[\rho_{\uparrow}, \rho_{\downarrow}] = \int d\vec{r} \rho(\vec{r}) \epsilon_{xc}[\rho, \zeta] \quad (34)$$

The *Generalized Gradient Approximation* (GGA) introduces a correction for electronic density variations by including the gradient of the density. GGA functionals are used in the description of the E_{xc} term for molecules. The most famous GGA functionals are those parameterized by Perdew, Burke, and Ernzerhof referred to as *PBE functionals* [51].

$$E_{xc}^{GGA} = \int d\vec{r} \rho(\vec{r}) V_{xc}(\rho_{\uparrow}, \rho_{\downarrow}, \nabla \rho_{\uparrow}, \nabla \rho_{\downarrow}) \quad (35)$$

5. Plane Waves

One strategy to solve the Kohn-Sham equations is to explore the periodicity of crystal structures and expand the orbitals $\phi_i(\vec{r})$ in plane-waves using *Fourier Transform* [43]. In a periodic potential, the *Bloch Theorem* states that we can write the solution of the Schrodinger Equation as the product of a plane wave and some periodic function $f(\vec{k})$ whose period equals that of the system in the reciprocal lattice [42]. The *Reciprocal Lattice* is build upon the direct lattice vectors \vec{a}_1 , \vec{a}_2 and \vec{a}_3 of a crystal by defining the *primitive reciprocal lattice vectors* [52]:

$$\vec{b}_1 = \frac{2\pi}{\Omega} \vec{a}_2 \times \vec{a}_3, \quad \vec{b}_2 = \frac{2\pi}{\Omega} \vec{a}_3 \times \vec{a}_1, \quad \vec{b}_3 = \frac{2\pi}{\Omega} \vec{a}_1 \times \vec{a}_2 \quad (36)$$

where $\Omega = \vec{a}_1 \cdot (\vec{a}_2 \times \vec{a}_3)$ denotes the primitive unit cell volume. The units for these vectors are the reciprocal of those from a_j , thus the name. Reciprocal vectors increase as direct lattice vectors becomes smaller. The vectors \vec{b}_j are defined to satisfy the condition:

$$\vec{a}_i \cdot \vec{b}_j = 2\pi\delta_{ij} \quad (37)$$

where δ_{ij} is the *Kronecker delta*. They define the so-called reciprocal lattice vectors \vec{G} :

$$\vec{G} = m_1\vec{b}_1 + m_2\vec{b}_2 + m_3\vec{b}_3, \quad m_k \in \mathbb{Z} \quad (38)$$

which automatically satisfy the periodic conditions for a plane-wave and its gradient describing a crystal with Bravais vector $\vec{R} = n_1\vec{a}_1 + n_2\vec{a}_2 + n_3\vec{a}_3$ (n_i is an integer). This can be seen by the following set of equations:

$$e^{i\vec{G}\cdot(\mathbf{r}+\vec{R})} = e^{i\vec{G}\cdot\mathbf{r}} \quad (39)$$

$$\nabla_{\mathbf{r}} e^{i\vec{G}\cdot(\mathbf{r}+\vec{R})} = \nabla_{\mathbf{r}} e^{i\vec{G}\cdot\mathbf{r}} \quad (40)$$

According to Bloch's Theorem, we can write a Khon-Sham orbital as:

$$\phi_i(\vec{r}) = f(\vec{k})e^{i\vec{k}\cdot\mathbf{r}} \quad (41)$$

where \vec{k} are vectors in the reciprocal space. Then we expand the function $f(\vec{k})$ using plane-waves:

$$f(\vec{k}) = \sum_{\vec{G}} c(\vec{G})e^{i\vec{G}\cdot\mathbf{r}} \quad (42)$$

summing over all the \vec{G} 's. The orbital is rewritten as:

$$\phi_{i\vec{k}}(\vec{r}) = \sum_{\vec{G}} c(\vec{k} + \vec{G})e^{i(\vec{k}+\vec{G})\cdot\mathbf{r}} \quad (43)$$

In practical implementations, this sum is truncated. The *plane-waves kinetic energy cutoff* is defined to determine the largest reciprocal lattice vector (\vec{G}_{max}) used in the Fourier transform. This vector limits the kinetic energy:

$$E_{cut} = \frac{\hbar^2}{2m} |\vec{G}_{max}|^2 \quad (44)$$

therefore, only the plane-waves with kinetic energy smaller than E_{cut} are included in the plane-wave basis set [42]. The summation becomes:

$$\phi_{i\vec{k}}(\vec{r}) = \sum_{|\vec{k}+\vec{G}| \leq G_{max}} c(\vec{k} + \vec{G})e^{i(\vec{k}+\vec{G})\cdot\mathbf{r}} \quad (45)$$

Plane waves simplify the calculations because they are much simpler to handle and more effective for dealing with periodic boundary conditions [43]. Also Fourier transforms are efficiently evaluated with *Fast Fourier Transform* (FFT) algorithms [53].

The smallest portion of the volume in the direct space capable of reproducing the entire lattice by symmetry operations is called *Wigner-Seitz cell* [52]. In the reciprocal space, it is called the *Brillouin Zone* (BZ). In DFT, integrals of functions over the Brillouin Zone appears very often. Numerical methods are employed to solve these integrals by discretizing the BZ into the so-called k-points grids [42].

We must choose this grid carefully to keep the consumption of computational resources practical. The most common method is the Monkhorst-Pack grid, defined as a cubic grid in which each direction of the reciprocal lattice is evenly spaced [54]. The number of k-points in each direction is not necessarily equal.

6. Pseudopotentials

Valence electrons dominate the properties of chemical bonding. It is reasonable to treat tightly bounded core electrons as if they were in an isolated atom [42]. We describe the chemical bonding environment only by the properties of valence electrons of the atoms in it. However, simply eliminating core electrons does not reproduce the correct nodal structure of the electronic wave function near the core. The pseudopotential approach sets a cutoff radius (r_c) defining a region ($0 < r < r_c$) in which the wavefunction is replaced with a smooth, nodeless function. This new function must yield the same electronic density and reproduce the slope of the wave function in $r = r_c$ [43].

We construct pseudopotentials by taking a single isolated atom. However, the resulting pseudopotential is adequate for any chemical environment without any additional adjustments (*transferability*). The details of a pseudopotential include the minimum cutoff energy for a specific element. The value of this energy defines its *softness*. Higher cutoff values define *hard* pseudopotentials, while more computationally efficient and lower cutoff pseudopotentials are said to be *soft* [42]. DFT codes include libraries for pseudopotentials with entries for almost every element in the periodic table. The most common types are the *norm-conservative* and *ultrasoft* pseudopotentials [55].

7. The rVV10 Exchange and Correlation Functional

Standard DFT does not account for van der Waals (vdW) interactions, present in layered TMDs. In this work, we employ the revised Vydrov and Van Voorhis (rVV10) exchange and correlation functional because it is self-consistent and implemented on several plane-waves based DFT codes. A brief discussion is presented next.

The Vydrov and Van Voorhis correlation functional (VV10) is a non-local functional that describes long-range dispersion interactions (van der Waals) through the electronic density (ρ) as an input, also describing short-ranges interactions in a very simplified manner. By adding a term proportional to the number of electrons (Eq. 48) to the Dion non-local correlation energy (E_c , Eq. 46) [56], the description for uniform densities remain unchanged. The VV10 can be incorporated to exchange and correlation functionals without changing its description for a uniform gas of electrons [57].

$$E_c^{nl} = \frac{\tilde{c}}{2} \int \int \rho(\vec{r}) \Phi(\rho, \rho', j\vec{r}, j\vec{r}', \vec{R}) \rho(\vec{r}') d\vec{r} d\vec{r}' \quad (46)$$

$$E_{c-nl}^{VV10} = \beta N + E_c^{nl} \quad (47)$$

$$= \int d\vec{r} \rho(\vec{r}) \left[\beta + \int d\vec{r}' \rho(\vec{r}') \Phi^{VV10}(\vec{r}, \vec{r}') \right] \quad (48)$$

VV10 depends on less empirical parameters, its more precise and poses a relatively simple and efficient implementation. Vydrov and Van Voorhis functional was implemented in Gaussian base codes such as Q-Chem, Orca, and ERKALE [58]. The kernel (Φ) of this functional is given by:

$$\Phi^{VV10} = \frac{3}{2} \kappa^{-\frac{3}{2}} \kappa'^{-\frac{3}{2}} \left(\frac{gg'}{\kappa\kappa'} \left[\sqrt{\frac{\kappa}{\kappa'}} \frac{g}{\kappa} + \sqrt{\frac{\kappa'}{\kappa}} \frac{g}{\kappa'} \right] \right)^{-1} \quad (49)$$

$$\kappa = \frac{3\pi b}{(576\pi)^{\frac{1}{6}}} \rho^{\frac{1}{6}}, \quad \kappa' = \frac{3\pi b}{(576\pi)^{\frac{1}{6}}} \rho'^{\frac{1}{6}} \quad (50)$$

where g is a function of the plasma frequency (ω_0) and the distance $j\vec{r} - \vec{r}'j$. b its an empirical parameter [58].

Sabatini and coworkers studied this kernel concluding that the approximation $\sqrt{\frac{\kappa}{\kappa'}} \approx 1$ would be valid in a variety of situations. This factor would only differ from 1 in cases where the interacting charge densities are very far apart. Even in this scenario, the difference would be small [59]. Introducing this approximation, we can interpolate the kernel Φ by the Romám-Pérez-Soler (RPS) method [60], enabling its implementation in periodic plane waves-based codes such as Quantum

Espresso, CP2K e ONETEP [59]. The *revised VV10* (rVV10) kernel is:

$$\Phi^{rVV10} = \frac{3}{2} \kappa^{-\frac{3}{2}} \kappa'^{-\frac{3}{2}} \left(\frac{gg'}{\kappa\kappa'} \left[\frac{g}{\kappa} + \frac{g'}{\kappa'} \right] \right)^{-1} \quad (51)$$

Eq. 51 can be written in a simpler manner, in terms of the auxiliary function:

$$q(\vec{r}) = \frac{\omega_0(\rho, j^r \rho f)}{\kappa} \quad (52)$$

and in terms of $R = j\vec{r} \quad \vec{r}^j j$, the kernel Φ^{rVV10} is rewritten as:

$$\Phi^{rVV10} = \frac{3e^4}{2m^2} \frac{1}{(qR^2 + 1)(q'R^2 + 1)(qR^2 + q'R^2 + 2)} \quad (53)$$

The exchange and correlation energy is given by:

$$E_{xc}^{rVV10} = E_x^{rPW86} + E_c^{LDA} + E_{c-nl}^{rVV10} \quad (54)$$

where E_x^{rPW86} is the exchange energy for the refitted Perdew-Wang functional. E_c^{LDA} is the correlation energy for the LDA approximation, according to the Perdew-Wang parameterization. E_{c-nl}^{rVV10} is the exchange and correlation energy, given by Eq. 48 with the kernel Φ defined in Eq. 53 [59].

2.2. Computational Procedures

The *ab initio* calculations performed in this work were carried out using the DFT formalism implemented in Quantum Espresso (QE) [61, 62]. QE is an open-source distribution of integrated computational codes for DFT calculations based on Plane Waves and pseudopotentials [61]. To account for the weak van der Waals interlayer interactions on the *TiSe₂*, the (rVV10) functional was employed. The Kohn-Sham (KS) orbitals were expanded using Plane Waves basis set with kinetic energy cutoff (E_{cut}) of 816 eV. The pseudopotentials were collected from the Standard Solid State Pseudopotentials (SSSP) library [63, 64].

Geometry optimization was carried out with the unit-cell from the Materials Project [65]. We performed Brillouin Zone (BZ) integration by studying the total forces on the atoms as a function of the Monkhorst-Pack [54] *k-point* grid used to sample the BZ. The total force difference between a sample with a grid of $n \times n \times n$ and one with $(n + 1) \times (n + 1) \times (n + 1)$ was calculated until their difference was smaller than $0.0257 \text{ eV}/\text{\AA}$ (10^{-3} Ry/Bohr). Then, the unit cell was allowed to relax (with variable cell volume) until the total energy between two Kohn-Sham self-consistent steps was smaller than 10^{-6} eV . Convergence thresholds for ionic steps were set to 10^{-3} eV in

energy and 0.0257 eV/\AA in forces. Surface energy (E_S) was studied as a function of the number of layers, calculated by the standard method [66]:

$$E_S = \frac{E_{slab}(n) - nE_{bulk}}{2A} \quad (55)$$

where $E_{slab}(n)$ is the energy of a $(1 \times 1 \times n)$ slab, E_{bulk} is the energy of a bulk unit cell and A the surface area of the primitive unit cell. We used Boettger and Gay methods (discussed in detail in Ref. [66]) to estimate E_{bulk} and calculate E_S for $(1 \times 1 \times n)$ slabs, with n ranging from 1 to 7, comparing the three methods.

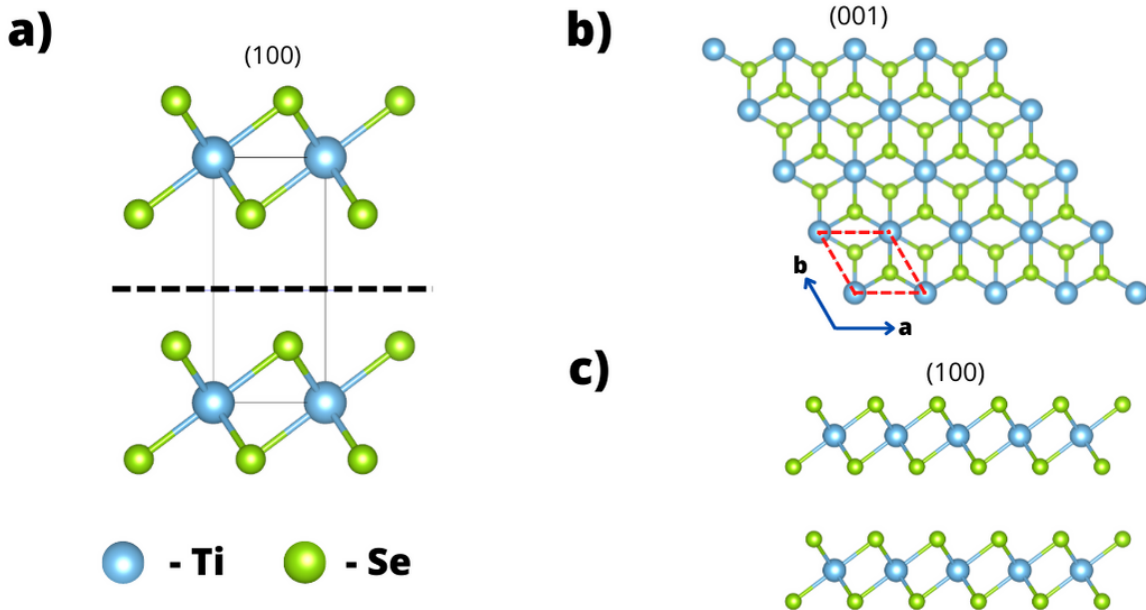


FIG. 4: In a) (100) view of the $TiSe_2$ unit cell. The dashed line indicates the direction of cleavage (001). In b) the (001) surface of the 4×4 supercell of $TiSe_2$. The unit of repetition is highlighted in the red dashed parallelogram. In c) the (100) view of the 4×4 supercell depicting the stacking of two layers.

The optimized 1T- $TiSe_2$ unit cell was repeated 4 times in the a and b lattice directions, forming a 4×4 supercell. Then, it was cleaved in the 001 plane using the *Atomic Simulation environment* (ASE) [67, 68]. The resulting supercells were stacked to form a 5-layer slab. Fig.4 illustrate this procedure. To avoid interactions between the boundary layers we added a vacuum of 15\AA on both sides of the slabs. The doped structures were constructed by substituting one Ti atom at the top layer by Pt . Slab geometry was conducted by fixing the bottom layer and relaxing the structure allowing its volume to change. Self consistent and ionic convergence thresholds were set to the same values used in the unit cell optimization. In this step, we used a Γ centered k-point grid to optimize computational resources consumption.

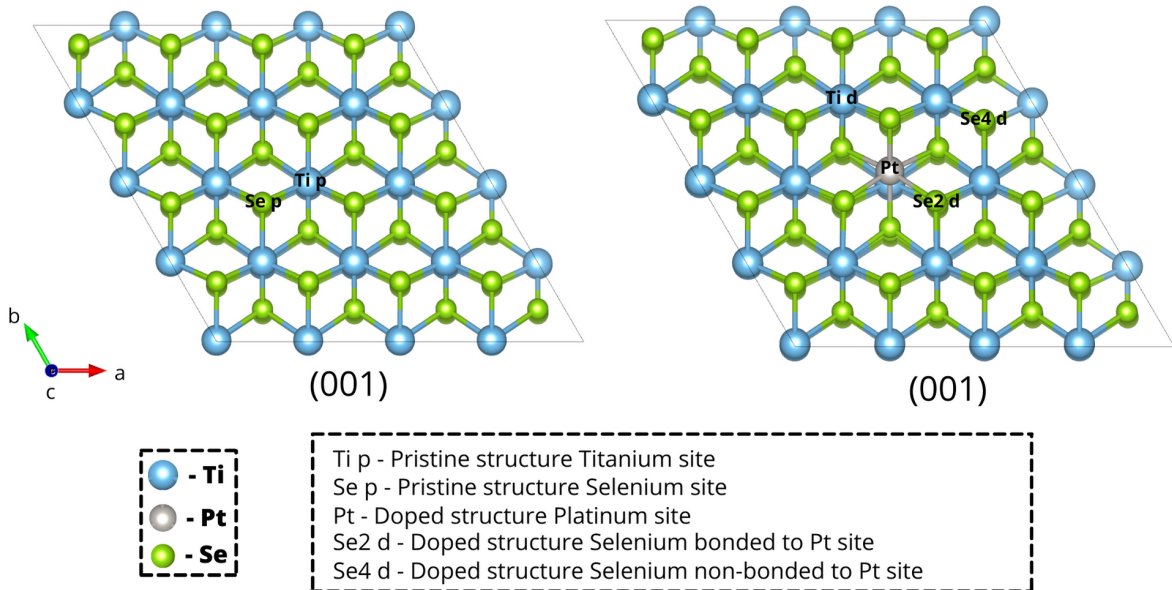


FIG. 5: Selected sites to adsorb Hydrogen. On the left, the pristine TiSe_2 slab and the two $Ti\ p$, $Se\ p$ selected sites. On the right the selected sites and the non-equivalent Se sites labeled as $Se2\ d$, which is the atoms bonded to Pt and $Se4\ d$ an atom not bonded to Pt .

With the optimized slabs, a H atom was placed in the top layer sites (001 surface or basal plane) at a distance of 1\AA from the atoms but slightly tilted, so that the orbital could overlap correctly to form a bond. For the pristine TiSe_2 , one Ti and Se sites were investigated ($Ti\ p$ and $Se\ p$, respectively). For the PtTiSe_2 surface (with one Ti atom substituted for Pt) the Ti , Pt and two different Se sites were investigated. We selected the closest Ti atom not bonded to Pt ($Ti\ d$ site). For the Se , we selected one atom bonded to Pt ($Se2\ d$) and a non-bonded ($Se4\ d$) atom, so the effects of different electronic neighborhood could be studied. The selected sites are summarized and labeled in Fig. 5.

1. Computational Model for HER

We modeled the HER by the *Computational Hydrogen Electrode* (CHE). Proposed by Nørskov and co-workers in 2004, this model allows us to analyze the thermodynamics of electrochemical reactions in terms of the free energies of elementary steps [69]. These free energies are obtained by DFT calculations of intermediates adsorption. At $U = 0V$ and $pH = 0$, the free-energy for a particularly intermediate is given by:

$$\Delta G_i = \Delta E_{i^*} + \Delta E_{ZPE} - T\Delta S_i \quad (56)$$

ΔE_{ZPE} and ΔS are the vibrational *zero-point energy* and entropy differences, respectively. ΔE_{i^*} represents the binding energy of the i -th intermediate on the surface. In the acid HER, the intermediate step is the adsorbed proton on the catalyst surface - H^* (see Eqs 5-7). The Hydrogen Binding Energy is calculated by [22, 23]:

$$\Delta E_{H^*} = E_{*+H} - \left(E_* + \frac{1}{2} E_{H_2} \right) \quad (57)$$

where E_{*+H} denotes the energy of the catalyst with adsorbed H and E_* is the energy of the catalyst. In the CHE model, protons and electrons are in equilibrium with H_2 in the reaction $H^+ + e^- \rightleftharpoons 1/2 H_2$ [69, 70]. Therefore, we use the energy of $H^+ + e^-$ as half the energy of a H_2 molecule.

Following the works of Nørskov [23] and Deng [33], the contribution of the zero point energy and entropy for metal catalysts can be approximated to 0.24 eV. Therefore the equation used to calculate the H adsorption free-energy variation is:

$$\Delta G_{H^*} = \Delta E_{H^*} + 0.24 eV \quad (58)$$

As our energy convergence threshold for ionic steps are 10^{-3} Ry (order of 10^{-2} eV) ΔG_{H^*} has two decimal digits.

3. RESULTS

The optimization of k-points resulted in a force convergence for a $5 \times 5 \times 5$ Monkhorst-pack grid (Fig. 6a,b). Our surface energy study showed that the difference in E_S becomes smaller than 0.001 J/m² for slabs with more than 5 layers (inclusive). We found that the Standard and Boettger's methods are in good agreement while the Gay method (fit method) got closer to the standard curve, as we decreased the number of points used to estimate E_{bulk} . These results are summarized in Fig. 6.c. The curves labeled as "Fit. n0" corresponds to E_S calculated using different approximations for E_{bulk} . Lattice parameters and angles for the optimized unit-cell are shown in Tab. I. The obtained parameters are in good agreement with experimental values reported by Chen *et al* [39].

Tab. II shows the Gibbs free energy variation of H adsorption (ΔG_{H^*}) for both pristine and doped 5-layer slabs. We found that Ti and Pt sites are metastable: the H atoms initially adsorbed on them moved to Se sites nearby. This result was observed in both the pristine and doped slabs (in the case of Ti sites). Our calculations for free energy variation showed a slight change in the ΔG_{H^*} towards zero for the doped Se sites, indicating the enhancement of activity in the doped

	a (Å)	b (Å)	c (Å)	α (°)	β (°)	γ (°)
DFT	3.60	3.60	6.09	89.61	90.02	120.07
Exp.	3.54	3.54	6.01	90	90	120

TABLE I: Unit cell lattice constants from DFT calculation (via geometry optimization) and experimental values obtained from Ref. [39]

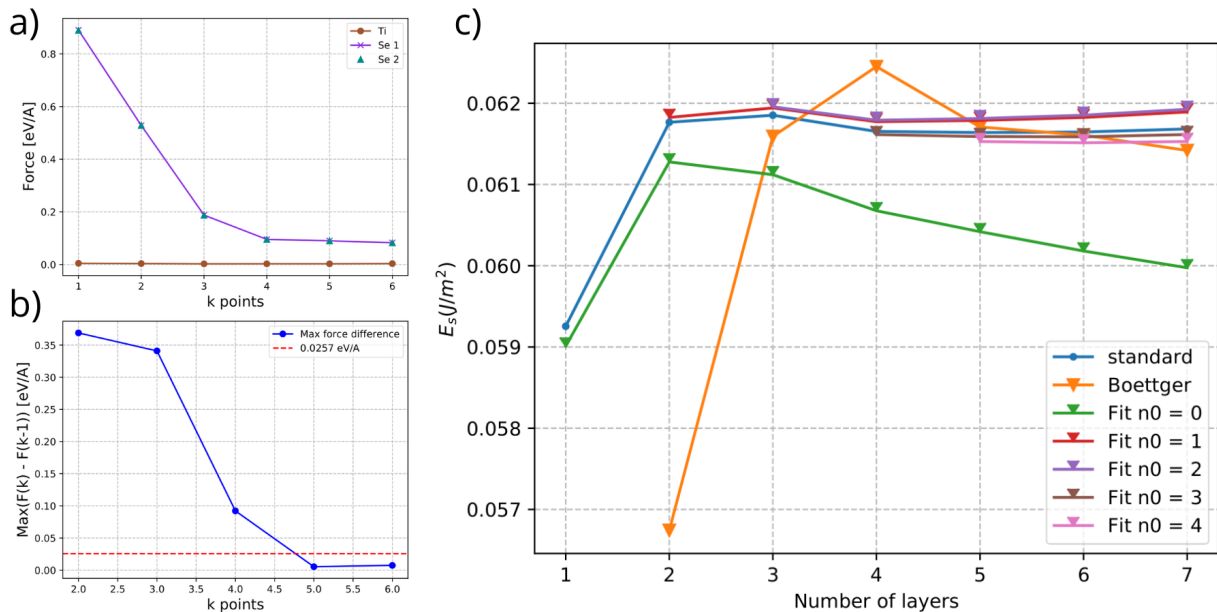


FIG. 6: Optimization studies for the unit cell. In a) and b) the forces on the atoms and the maximum difference between two consecutive ionic steps (respectively) are shown. In c) the surface energy obtained by the Standard, Boettger and Gay methods discussed in detail in Ref. [66].

slab¹. However, the low amount of Pt dopants in the 5-layer slab softens the effects of the doping. To investigate the effects of higher amounts of Pt dopants, we constructed a 2 × 2 monolayer of $TiSe_2$. In this smaller structure, the direct substitution of Ti atoms results in a higher Pt to Ti ratio.

We performed geometry optimization calculations employing the same methods used for the 5-layers slabs, using the same convergence threshold values. Adsorption calculations were performed in the basal plane sites shown in Fig. 7. We found positive values for ΔG_{H^*} in both pristine and doped slabs, in agreement with the results for H adsorption on the basal plane of TMDs monolayer reported by Deng *et al* [33] and Tsai *et al* [71]. Ti sites were found to be metastable as well, in

¹ The calculations for the Se4 d site still running.

Site	$\mathbf{E}_{\mathbf{H}^*}$ (eV)	$\Delta\mathbf{E}_{\mathbf{H}^*}$ (eV)	$\Delta\mathbf{G}_{\mathbf{H}^*}$ (eV)
Ti p	-225563.85	N/A	N/A
Se p	-225564.04	-1.72	-1.48
Ti d	-226805.05	N/A	N/A
Pt	-226805.18	N/A	-N/A
Se2 d	-226805.97	-1.66	-1.42
Se4 d	-226805.86	-1.55	-1.31

TABLE II: Resulting ground-state energies for the 5-layers slabs with adsorbed H and corresponding adsorption free energies calculated by Eq. 58 for each site.

agreement with the results reported by Deng et al [33] for the MoS_2 . The pristine Se site on the monolayer adsorbed H with $\Delta G_{H^*} = 0.99$ eV, reasonably close to the value of 0.81 eV reported by Tsai *et al* [71]. Unlike the 5-layers slab, the Pt site on the monolayer successfully adsorbed H with the best ΔG_{H^*} (+0.23 eV) among all the investigated sites. On the doped monolayer, the Se sites presented a significant change in the ΔG_{H^*} of 45% in the case of the Se site non-bonded to Pt (Se 4 d) and 65% in the case of the Se site bonded to Pt (Se 2 d). These findings are summarized in the Tab. III.

We elaborated a qualitative Charge density difference analysis in the adsorbed H by subtracting the charge density of the system with adsorbed H and the charge densities of the 2 × 2 monolayer and a H atom on a system with the same lattice parameters. The variation of the charge density is given by the formula:

$$\Delta\rho = \rho(TiSe_2 + H) - (\rho(TiSe_2) + \rho(H)) \quad (59)$$

The isosurfaces corresponding to the charge accumulation and depletion are show in Fig. 8. We observed a charge accumulation ($\Delta\rho < 0$) in the Se-H bond region, indicating charge transfer in the process of adsorption. This was observed in both the pristine and doped structures.

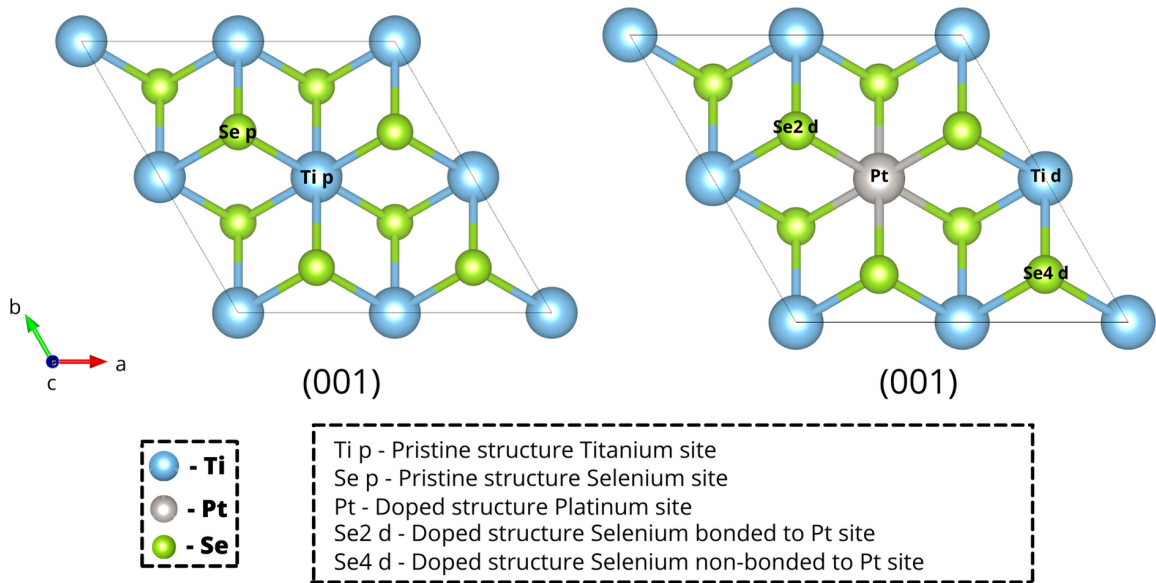


FIG. 7: Selected sites for H adsorption calculations on the pristine and doped 2×2 monolayer slabs. Labels are similar to that of Fig. 5.

Site	E_{H^*} (eV)	ΔE_H (eV)	ΔG_{H^*} (eV)
Ti p	-11264.45	N/A	N/A
Se p	-11264.35	0.75	0.99
Ti d	-12505.95	N/A	N/A
Pt	-12506.28	-0.01	0.23
Se2 d	-12506.19	0.08	0.32
Se4 d	-12505.97	0.30	0.54

TABLE III: Ground-state energies of 2×2 monolayer slabs with adsorbed H and corresponding adsorption free energies for each site.

We compiled the results of Tables II and III to elaborate the free energy diagrams in Fig. 9. The central plateaus indicate the ΔG for the adsorbed H (H^*) intermediate state. The activity of a site is better as ΔG_{H^*} gets closer to zero. In the case of 5-layer slabs, Pt introduction results in a slight but perceptible enhancement in the activity on Se sites. On the 2×2 monolayer, where the Pt to Ti ratio is considerably higher, the catalytic activity of Se sites is improved. The Se site bonded to Pt (Se 2) is the most affected by the presence of the heteroatom, as seen by the significant change on its ΔG_{H^*} towards zero. These results are notable and suggest that the effects of doping are related to the amount of heteroatom in the structure.

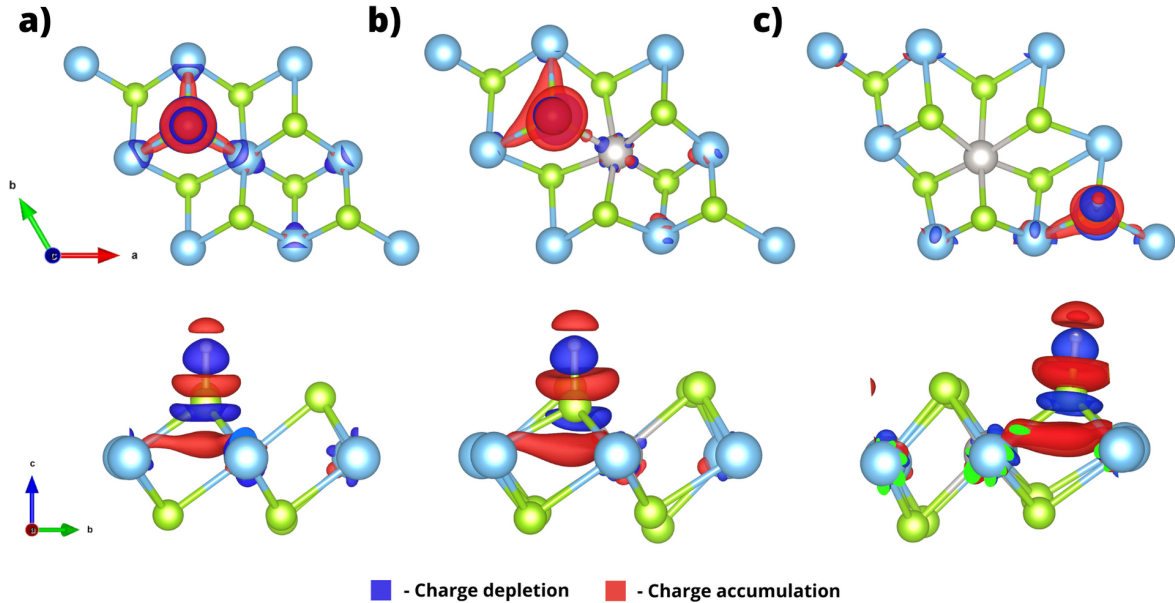


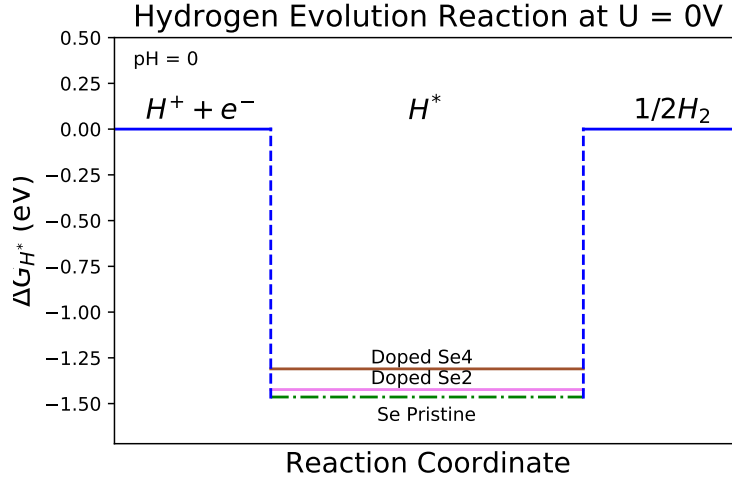
FIG. 8: Top (001) and side (100) view of charge density difference plots. In a) Se pristine site, in b) Se2 and c) Se4 doped sites on the monolayers. Charge accumulation and depletion regions are labeled in red and blue, respectively.

4. CONCLUSIONS

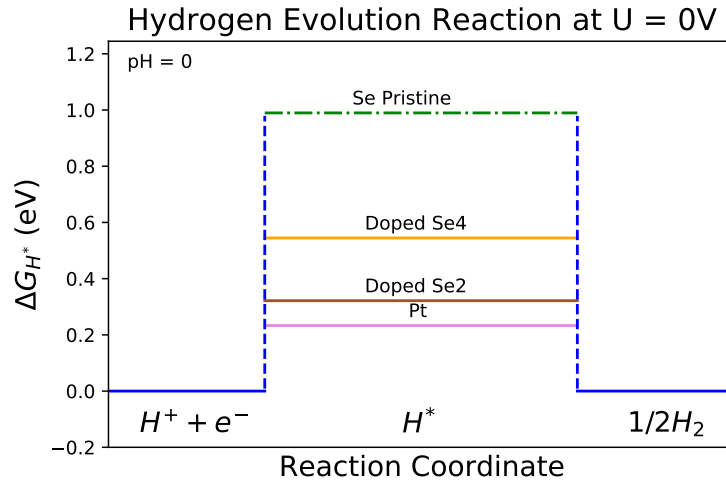
In this work, we investigated the catalytic activity of $TiSe_2$ on HERs by first principles calculations based on DFT. Our study included k-point and slab surface energy convergence analysis and we also performed geometry optimization and adsorption energy calculations. The optimized unit cell lattice constants were found to be in good agreement with experimental values.

We employed the Computational Hydrogen Electrode (CHE) to model the electrochemical HER and investigated the catalytic activity of $TiSe_2$ using the Gibbs free energy variation of intermediate states. Our calculations with 5 layer slabs indicated that Ti and Pt sites are metastable. We observed a slight change in the ΔG_{H^*} of the doped Se sites, indicating an enhancement of activity. The low amount of Pt atoms in the 5-layer slab motivated the study of a smaller structure with a higher amount of dopants. To simulate higher amount of heteroatoms, we performed similar calculations on a 2×2 monolayer of $TiSe_2$.

Our calculations with the monolayer confirmed that the Ti sites are metastable. However, the Pt sites adsorbed H with $\Delta G_{H^*} = 0.23$ eV, being the closest value to zero among all the investigated sites. The introduction of Pt resulted in a significant change of the ΔG_{H^*} for Se sites, with the larger impact observed in the Se atom bonded to Pt. As seen by our free energy diagrams, introduction of Pt tends to push the ΔG_{H^*} towards zero, indicating an enhancement in



(a)



(b)

FIG. 9: Gibbs free energy variation diagrams for (a) 5-layers slabs and (b) the diagram for the 2×2 monolayer. The dash-dotted and solid lines represents the pristine and doped slabs, respectively.

the catalytic activity of $1T-TiSe_2$. This work contributes to the development of new catalyst for HER and for the consolidation of doping as an effective strategy to improve the catalytic activity of TMDs in HERs.

5. ACKNOWLEDGMENTS

I cannot express my gratitude to my family for all the support during these undergrad years, especially in the last two years of the pandemic. Their efforts enabled each step of this journey! I am

deeply indebted to Professor Pedro Autreto, whose patience and dedication while supervising me were instrumental to this project. I also had the great pleasure to work with Lanna Lucchetti, whose invaluable suggestions and insights are very much appreciated. Thanks to my fellow GEEDAIs for the technical support and insightful discussions at our weekly meetings. My sincere thanks to CCM UFABC for all the computational resources provided.

References

- [1] B. Hinnemann, P. G. Moses, J. Bonde, K. P. Jørgensen, J. H. Nielsen, S. Horch, I. Chorkendorff, and J. K. Nørskov, *Journal of the American Chemical Society* **127**, 5308 (2005).
- [2] T. F. Jaramillo, K. P. Jørgensen, J. Bonde, J. H. Nielsen, S. Horch, and I. Chorkendorff, *Science* **317**, 100 (2007).
- [3] H. Ritchie and M. Roser, *Our World in Data* (2020), <https://ourworldindata.org/energy>.
- [4] M. V., P. Zhai, A. Pirani, S. Connors, C. Péan, S. Berger, N. Caud, Y. Chen, L. Goldfarb, M. Gomis, M. Huang, K. Leitzell, E. Lonnoy, J. Matthews, T. Maycock, T. Waterfield, O. Yelekçi, R. Yu, , and B. Z. (eds.), “Ipcc, 2021: Summary for policymakers. in: Climate change 2021: The physical science basis,” (in press).
- [5] K. T. Møller, T. R. Jensen, E. Akiba, and H. wen Li, *Progress in Natural Science: Materials International* **27**, 34 (2017).
- [6] K. Mazloomi and C. Gomes, *Renewable and Sustainable Energy Reviews* **16**, 3024 (2012).
- [7] G. Nicoletti, N. Arcuri, G. Nicoletti, and R. Bruno, *Energy Conversion and Management* **89**, 205 (2015).
- [8] P. J. Megia, A. J. Vizcaino, J. A. Calles, and A. Carrero, *Energy and Fuels* **35**, 16403 (2021).
- [9] A. M. Oliveira, R. R. Beswick, and Y. Yan, *Current Opinion in Chemical Engineering* **33**, 100701 (2021).
- [10] S. Wang, A. Lu, and C. J. Zhong, *Nano Convergence* **8** (2021), 10.1186/s40580-021-00254-x.
- [11] F. Safari and I. Dincer, *Energy Conversion and Management* **205**, 112182 (2020).
- [12] A. Lasia, *International Journal of Hydrogen Energy* **44**, 19484 (2019).
- [13] K. Zeng and D. Zhang, *Progress in Energy and Combustion Science* **36**, 307 (2010).
- [14] L. Lin, P. Sherrell, Y. Liu, W. Lei, S. Zhang, H. Zhang, G. G. Wallace, and J. Chen, *Advanced Energy Materials* **10**, 1 (2020).
- [15] D. Strmcnik, M. Uchimura, C. Wang, R. Subbaraman, N. Danilovic, D. Van Der Vliet, A. P. Paulikas, V. R. Stamenkovic, and N. M. Markovic, *Nature Chemistry* **5**, 300 (2013).
- [16] Q. Liang, G. Brocks, and A. Bieberle-Hütter, *JPhys Energy* **3**, 0 (2021).
- [17] J. Zhu, L. Hu, P. Zhao, L. Y. S. Lee, and K.-Y. Wong, *Chemical Reviews* **120**, 851 (2020).
- [18] Z. Wang, M. T. Tang, A. Cao, K. Chan, and J. K. Nørskov, *The Journal of Physical Chemistry C* , [acs.jpcc.1c10436](https://doi.org/10.1021/acs.jpcc.1c10436) (2022).
- [19] K. Zhu, C. Li, Z. Jing, X. Liu, Y. He, X. Lv, Y. Wang, and K. Liu, *FlatChem* **18**, 100140 (2019).
- [20] V. R. Stamenkovic, D. Strmcnik, P. P. Lopes, and N. M. Markovic, *Nature Materials* **16**, 57 (2016).
- [21] N. Dubouis and A. Grimaud, *Chemical Science* **10**, 9165 (2019).
- [22] Y. Wang, W. Qiu, E. Song, F. Gu, Z. Zheng, X. Zhao, Y. Zhao, J. Liu, and W. Zhang, *National*

- Science Review* **5**, 327 (2018).
- [23] J. K. Nørskov, T. Bligaard, A. Logadottir, J. R. Kitchin, J. G. Chen, S. Pandelov, and U. Stimming, *Journal of The Electrochemical Society* **152**, J23 (2005).
- [24] C. Li and J. B. Baek, *ACS Omega* **5**, 31 (2020).
- [25] A. Devadoss, N. Srinivasan, V. Devarajan, A. N. Grace, and S. Pitchaimuthu, *2D Nanoscale Heterostructured Materials*.
- [26] Y. Qu, H. Pan, and C. T. Kwok, *Scientific Reports* **6**, 1 (2016).
- [27] G. Eda, H. Yamaguchi, D. Voiry, T. Fujita, M. Chen, and M. Chhowalla, *Nano Letters* **11**, 5111 (2011).
- [28] H. Saqib, S. Rahman, Y. Zhao, C. Cazorla, D. Errandonea, R. Susilo, Y. Zhuang, Y. Huang, B. Chen, and N. Dai, *Journal of Physical Chemistry Letters* **12**, 9859 (2021).
- [29] K. A. N. Duerloo, Y. Li, and E. J. Reed, *Nature Communications* **5**, 1 (2014).
- [30] H. H. Huang, X. Fan, D. J. Singh, and W. T. Zheng, *Nanoscale* **12**, 1247 (2020).
- [31] W. Zhao, J. Pan, Y. Fang, X. Che, D. Wang, K. Bu, and F. Huang, *Chemistry - A European Journal* **24**, 15942 (2018).
- [32] M. A. Lukowski, A. S. Daniel, F. Meng, A. Forticaux, L. Li, and S. Jin, *Journal of the American Chemical Society* **135**, 10274 (2013).
- [33] J. Deng, H. Li, J. Xiao, Y. Tu, D. Deng, H. Yang, H. Tian, J. Li, P. Ren, and X. Bao, *Energy and Environmental Science* **8**, 1594 (2015).
- [34] D. Voiry, J. Yang, and M. Chhowalla, *Advanced Materials* **28**, 6197 (2016).
- [35] F. J. Di Salvo, D. E. Moncton, and J. V. Waszczak, *Physical Review B* **14**, 4321 (1976).
- [36] A. F. Kusmartseva, B. Sipos, H. Berger, L. Forró, and E. Tutiš, *Physical Review Letters* **103**, 1 (2009).
- [37] A. Kumar, R. Sharma, S. Yadav, S. K. Swami, R. Kumari, V. N. Singh, S. Ojha, J. J. Schneider, R. Srivastava, and O. P. Sinha, *Dalton Transactions* **50**, 3894 (2021).
- [38] R. H. Friend, D. Jérôme, W. Y. Liang, C. Mikkelsen, and A. D. Yoffe, *Journal of Physics C: Solid State Physics* **10**, 705 (1977).
- [39] J. S. Chen, J. K. Wang, S. V. Carr, S. C. Vogel, O. Gourdon, P. Dai, and E. Morosan, *Physical Review B - Condensed Matter and Materials Physics* **91**, 1 (2015).
- [40] D. Zhang, G. Zhao, P. Li, Y. Zhang, W. Qiu, J. Shu, Y. Jiang, S. X. Dou, and W. Sun, *Chemistry - A European Journal* **24**, 1193 (2018).
- [41] D. L. Duong, M. Burghard, and J. C. Schön, *Physical Review B - Condensed Matter and Materials Physics* **92**, 1 (2015).
- [42] D. Sholl and J. Steckel, *Density Functional Theory: A Practical Introduction* (Wiley, 2011).
- [43] F. Giustino, *Materials Modelling Using Density Functional Theory: Properties and Predictions* (Oxford University Press, 2014).
- [44] P. Hohenberg and W. Kohn, *Phys. Rev.* **136**, B864 (1964).
- [45] K. Capelle, *Braz. J. Phys.* **36**, 1318 (2006).
- [46] W. Kohn and L. J. Sham, *Phys. Rev.* **140**, A1133 (1965).

- [47] J. Stewart, *Cálculo Volume 2: Tradução Da 8a. Edição Norte-Americana* (Pioneira Thompson Learning Ltda, 2017).
- [48] K. A. Baseden and J. W. Tye, *Journal of Chemical Education* **91**, 2116 (2014).
- [49] D. M. Ceperley and B. J. Alder, *Phys. Rev. Lett.* **45**, 566 (1980).
- [50] A. Zunger, J. P. Perdew, and G. L. Oliver, *Solid State Communications* **34**, 933 (1980).
- [51] J. P. Perdew, K. Burke, and M. Ernzerhof, *Physical Review Letters* **77**, 3865 (1996).
- [52] C. Kittel, *Introduction to Solid State Physics* (Wiley, 2004).
- [53] J. C. Schatzman, *SIAM Journal on Scientific Computing* **17**, 1150 (1996), <https://doi.org/10.1137/S1064827593247023> .
- [54] H. J. Monkhorst and J. D. Pack, *Phys. Rev. B* **13**, 5188 (1976).
- [55] R. M. Martin, “Pseudopotentials,” in *Electronic Structure: Basic Theory and Practical Methods* (Cambridge University Press, 2004) p. 204–232.
- [56] M. Dion, H. Rydberg, E. Schröder, D. C. Langreth, and B. I. Lundqvist, *Phys. Rev. Lett.* **92**, 246401 (2004).
- [57] O. A. Vydrov and T. Van Voorhis, *Journal of Chemical Physics* **133**, 1 (2010), 1009.1421 .
- [58] N. Mardirossian, L. Ruiz Pestana, J. C. Womack, C. K. Skylaris, T. Head-Gordon, and M. Head-Gordon, *Journal of Physical Chemistry Letters* **8**, 35 (2017).
- [59] R. Sabatini, T. Gorni, and S. De Gironcoli, *Physical Review B - Condensed Matter and Materials Physics* **87**, 4 (2013).
- [60] G. Román-Pérez and J. M. Soler, *Physical Review Letters* **103**, 1 (2009).
- [61] P. Giannozzi, S. Baroni, N. Bonini, M. Calandra, R. Car, C. Cavazzoni, D. Ceresoli, G. L. Chiarotti, M. Cococcioni, I. Dabo, A. D. Corso, S. de Gironcoli, S. Fabris, G. Fratesi, R. Gebauer, U. Gerstmann, C. Gougoussis, A. Kokalj, M. Lazzeri, L. Martin-Samos, N. Marzari, F. Mauri, R. Mazzarello, S. Paolini, A. Pasquarello, L. Paulatto, C. Sbraccia, S. Scandolo, G. Sclauzero, A. P. Seitsonen, A. Smogunov, P. Umari, and R. M. Wentzcovitch, *Journal of Physics: Condensed Matter* **21**, 395502 (2009).
- [62] P. Giannozzi, O. Andreussi, T. Brumme, O. Bunau, M. B. Nardelli, M. Calandra, R. Car, C. Cavazzoni, D. Ceresoli, M. Cococcioni, N. Colonna, I. Carnimeo, A. D. Corso, S. de Gironcoli, P. Delugas, R. A. DiStasio, A. Ferretti, A. Floris, G. Fratesi, G. Fugallo, R. Gebauer, U. Gerstmann, F. Giustino, T. Gorni, J. Jia, M. Kawamura, H.-Y. Ko, A. Kokalj, E. Küçükbenli, M. Lazzeri, M. Marsili, N. Marzari, F. Mauri, N. L. Nguyen, H.-V. Nguyen, A. O. de-la Roza, L. Paulatto, S. Poncé, D. Rocca, R. Sabatini, B. Santra, M. Schlipf, A. P. Seitsonen, A. Smogunov, I. Timrov, T. Thonhauser, P. Umari, N. Vast, X. Wu, and S. Baroni, *Journal of Physics: Condensed Matter* **29**, 465901 (2017).
- [63] G. Prandini, A. Marrazzo, I. E. Castelli, N. Mounet, and N. Marzari, *npj Computational Materials* **4**, 72 (2018).
- [64] K. Lejaeghere, G. Bihlmayer, T. Björkman, P. Blaha, S. Blügel, V. Blum, D. Caliste, I. E. Castelli, S. J. Clark, A. D. Corso, S. de Gironcoli, T. Deutsch, J. K. Dewhurst, I. D. Marco, C. Draxl, M. Dulak, O. Eriksson, J. A. Flores-Livas, K. F. Garrity, L. Genovese, P. Giannozzi, M. Giantomassi, S. Goedecker,

- X. Gonze, O. Grånäs, E. K. U. Gross, A. Gulans, F. Gygi, D. R. Hamann, P. J. Hasnip, N. A. W. Holzwarth, D. Iuşan, D. B. Jochym, F. Jollet, D. Jones, G. Kresse, K. Koepernik, E. Küçükbenli, Y. O. Kvashnin, I. L. M. Locht, S. Lubeck, M. Marsman, N. Marzari, U. Nitzsche, L. Nordström, T. Ozaki, L. Paulatto, C. J. Pickard, W. Poelmans, M. I. J. Probert, K. Refson, M. Richter, G.-M. Rignanese, S. Saha, M. Scheffler, M. Schlipf, K. Schwarz, S. Sharma, F. Tavazza, P. Thunström, A. Tkatchenko, M. Torrent, D. Vanderbilt, M. J. van Setten, V. V. Speybroeck, J. M. Wills, J. R. Yates, G.-X. Zhang, and S. Cottenier, *Science* **351**, aad3000 (2016).
- [65] A. Jain, S. P. Ong, G. Hautier, W. Chen, W. D. Richards, S. Dacek, S. Cholia, D. Gunter, D. Skinner, G. Ceder, and K. a. Persson, *APL Materials* **1**, 11002 (2013).
- [66] T. Stirner, D. Scholz, and J. Sun, *Journal of Physics Condensed Matter* **32**, 0 (2020).
- [67] A. H. Larsen, J. J. Mortensen, J. Blomqvist, I. E. Castelli, R. Christensen, M. Dułak, J. Friis, M. N. Groves, B. Hammer, C. Hargus, E. D. Hermes, P. C. Jennings, P. B. Jensen, J. Kermode, J. R. Kitchin, E. L. Kolsbjerg, J. Kubal, K. Kaasbjerg, S. Lysgaard, J. B. Maronsson, T. Maxson, T. Olsen, L. Pastewka, A. Peterson, C. Rostgaard, J. Schiøtz, O. Schütt, M. Strange, K. S. Thygesen, T. Vegge, L. Vilhelmsen, M. Walter, Z. Zeng, and K. W. Jacobsen, *Journal of Physics: Condensed Matter* **29**, 273002 (2017).
- [68] S. R. Bahn and K. W. Jacobsen, *Comput. Sci. Eng.* **4**, 56 (2002).
- [69] J. K. Nørskov, J. Rossmeisl, A. Logadottir, L. Lindqvist, J. R. Kitchin, T. Bligaard, and H. Jónsson, *Journal of Physical Chemistry B* **108**, 17886 (2004).
- [70] D. R. Alfonso, D. N. Tafen, and D. R. Kauffmann, *Catalysts* **8** (2018), 10.3390/catal8100424.
- [71] C. Tsai, K. Chan, J. K. Nørskov, and F. Abild-Pedersen, *Surface Science* **640**, 133 (2015).
- [72] J. Deng, H. Li, J. Xiao, Y. Tu, D. Deng, H. Yang, H. Tian, J. Li, P. Ren, and X. Bao, *Energy Environ. Sci.* **8**, 1594 (2015).